Title
Experiments on convection in Earth’s core tangent cylinder

Journal
Earth and Planetary Science Letters, 212(1-2)

ISSN
0012-821X

Authors
Aurnou, Jonathan
Andreadis, Steven
Zhu, Lixin
et al.

Publication Date
2003-07-01

DOI
10.1016/s0012-821x(03)00237-1

Available online at www.sciencedirect.com

SCIENCE DIRECT®

EPSL

Earth and Planetary Science Letters 212 (2003) 119–134

www.elsevier.com/locate/epsl

Experiments on convection in Earth's core tangent cylinder

Jonathan Aurnou[a,*], Steven Andreadis[b], Lixin Zhu[b], Peter Olson[b]

[a] Department of Terrestrial Magnetism, Carnegie Institution of Washington, Washington, DC, USA
[b] Department of Earth and Planetary Sciences, Johns Hopkins University, Baltimore, MD, USA

Received 11 October 2002; received in revised form 25 February 2003; accepted 21 April 2003

Abstract

Results of thermal convection experiments in a rotating fluid with a geometry similar to the Earth's core tangent cylinder are presented. We find four different states. In order of increasing Rayleigh number, these are: (1) subcritical (no convection), (2) helical plumes around the tangent cylinder, (3) helical plumes throughout the tangent cylinder, and (4) fully three-dimensional convection. The convection generates a retrograde (westward) azimuthal thermal wind flow below the outer spherical boundary, with maximum velocity on the tangent cylinder. The velocity of the thermal wind scales with convective buoyancy flux $B=\alpha gq/\rho C_\mathrm{p}$ and Coriolis parameter $f=2\Omega$ as $U\simeq 2(B/f)^{1/2}$. Tangent cylinder convection can explain the origin of polar vortices beneath the core–mantle boundary inferred from geomagnetic secular variation, if a large fraction of the buoyancy produced by inner core solidification remains within the tangent cylinder, and also if the inner core growth rate is high. According to our experiments, the tangent cylinder can act as a reservoir for products of inner core growth, although the effect is probably far too small to detect from surface observations.

Keywords: core convection; tangent cylinder; geodynamo; thermal wind

1. Introduction

Flow in the outer core is constrained by the Earth's rotation. According to the Taylor–Proudman theorem, the vorticity in a rotating fluid tends to align with the rotation axis and the motion becomes nearly two-dimensional (2D; i.e. quasigeostrophic). The solid inner core has a major influence on this style of flow, because the nearly 2D vortices are inhibited from crossing the inner core tangent cylinder, an imaginary cylinder parallel to the spin axis and circumscribing the equator of the inner core. As shown in Fig. 1, the combination of the rotational constraint and the inner core acts to divide the outer core into three regions: outside the tangent cylinder and the northern and southern regions within the tangent cylinder, respectively.

Theoretical and experimental studies of rotating convection in spherical shells show strong tangent cylinder effects [1–3], as do most numerical dynamo models [4]. In rotating spherical shell convection, the fluid motions inside the tangent cylinder

---

* Corresponding author. Present addres: Department of Earth and Space Sciences, University of California, Los Angeles, USA. Tel.: +1-410-516-4659; Fax: +1-410-516-7933.

E-mail address: olson@jhu.edu (P. Olson).

0012-821X/03/$ – see front matter © 2003 Elsevier Science B.V. All rights reserved.
doi:10.1016/S0012-821X(03)00237-1

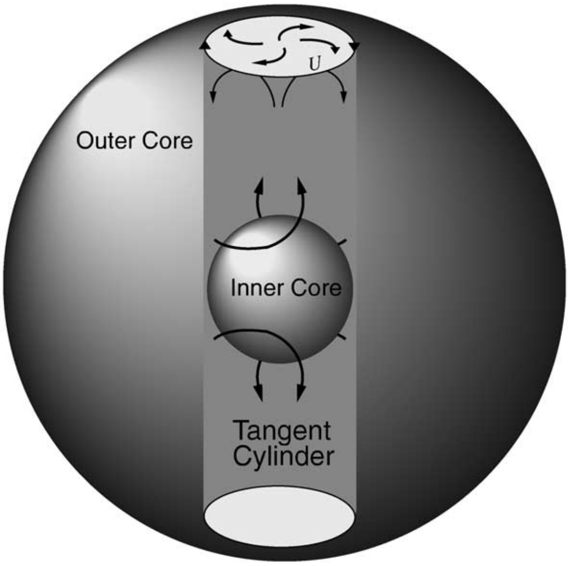

Fig. 1. Schematic of the Earth's core tangent cylinder region, including polar vortex associated with an azimuthal thermal wind.

usually include both small-scale and large-scale parts. The small-scale convective motion consists of rotationally aligned vortices with helical streamlines [5], which we call helical plumes. In addition, there are often larger-scale flows within the tangent cylinder, as illustrated schematically in Fig. 1. Typically the large-scale flow consists of a meridional component, with rising motion close to the pole and descending motion close to the tangent cylinder, plus an azimuthal baroclinic flow, which we refer to as thermal wind.

The thermal wind is prograde (eastward) above the inner core boundary and retrograde (westward) below the core–mantle boundary. In some dynamo models, thermal wind and meridional flow inside the tangent cylinder play important roles in magnetic field generation. The thermal wind shears the poloidal magnetic field, producing strong toroidal fields in the tangent cylinder region [6]. The convergence in the meridional flow near the inner core boundary concentrates the poloidal field, while the divergent flow below the core–mantle boundary advects the poloidal field toward lower latitudes, producing a polar minimum in the field intensity there [7]. Christensen et al. [8] have pointed out the similarity between the polar structure in numerical dynamo models and the present-day geomagnetic field on the core–mantle boundary. Anomalous rotation of the solid inner core is also related to the flows within the tangent cylinder. Numerical simulations in which the inner core freely rotates often show eastward flow above the inner core boundary, which tends to drag the inner core into eastward super-rotation [9,10].

Indirect evidence for azimuthal flow within the tangent cylinder comes from the secular changes in the propagation of seismic waves through the inner core. Secular changes in seismic wave travel times [11–13] and scattering [14] have been interpreted to indicate eastward inner core rotation relative to the mantle at 0.1–1° yr^{-1}. However, other studies find little or no secular change in the inner core seismic properties [15–18], so anomalous inner core rotation remains controversial.

Geomagnetic evidence for the tangent cylinder comes from the secular variation of the core field at high latitudes. The pattern of geomagnetic secular variation on the core–mantle boundary between 1980 Magsat and 2000 Oersted satellite missions indicates a westward polar vortex in each hemisphere, with peak angular velocities of about 1.5° yr^{-1} and average angular velocity in the tangent cylinder of about 0.5° yr^{-1} [19]. Previous studies identified a somewhat weaker polar vortex from the geomagnetic secular variation over the past 150 years [20,21].

In this paper we examine the convective motions in the tangent cylinder region, using experiments on convection above a heated cylinder in a rotating fluid with a hemispherical outer boundary. We determine the planform of motion at convective onset, and the speed and stability of the thermal wind produced by the convection. We propose a conceptual model for tangent cylinder convection in Section 2, including scaling laws for the motion. The controlling dimensionless parameters for tangent cylinder convection are introduced in Section 3. The experimental apparatus and methods are described in Section 4, and our results are presented in Section 5. In Sections 6 and 7 we discuss the implications of our experiments for the core.

2. Scaling laws for convection in the tangent cylinder

Here we propose a conceptual model for convection in the tangent cylinder of the core, based on analogy with convective chimneys in the oceans. In both the outer core and the oceans, the convection is driven by non-uniform buoyancy flux at a boundary, the fluid motions are turbulent, and the flow is subject to a combination of rotational and topographical constraints. The depths of the convecting regions are obviously very different in these two cases, but the typical aspect (width-to-depth) ratio of an ocean chimney is roughly comparable to the tangent cylinder in the core. There are other important differences, such as Lorentz forces and compressibility in the core, but we do not consider those effects here.

The following picture of ocean convection has been obtained from field, numerical, and experimental studies. Ocean convection is a transient phenomenon and occurs when locally cooled surface water becomes negatively buoyant, producing plumes that descend into the deep ocean [22]. As illustrated in Fig. 2, ocean convection typically occurs inside a cylindrical region called a chimney, which has the same lateral dimensions as the unstable surface water. Within the chimney, small-scale convective plumes develop from instabilities in the surface boundary layer and penetrate into the stably stratified deeper water. The plumes tend to be three-dimensional (3D) and turbulent when their transit time is less than a day. In cases where their transit time is greater than a day, the plumes are modified by Earth's rotation, forming quasi-columnar helical plumes, as illustrated in Fig. 2a. Helical plumes in the ocean have sinking motion along their centers, cyclonic vorticity near the surface where the horizontal velocity is convergent, and anticyclonic vorticity at the bottom where the horizontal velocity is divergent [23,24]. The particle trajectories in the plumes are helical, with the sign of the helicity reversing where the vorticity changes sign. As the buoyant fluid from the helical plumes fills the chimney region, a larger-scale lateral density gradient is established between the chimney and its surrounding environment. This density gradient generates a larger-scale baroclinic flow. Without rotation, the baroclinic flow would consist of a laterally spreading gravity current. With rotation, lateral spreading is inhibited and the fluid is deflected by the Coriolis force, producing a large-scale, azimuthal thermal wind. As in helical plumes, the vorticity of the thermal wind is anticyclonic where the horizontal velocity is divergent, and cyclonic where the horizontal velocity is convergent [24].

In ocean convection the thermal wind is cyclonic near the surface because the sinking of negatively buoyant surface water produces horizontal convergence there. The situation is different in the core, because the inner core is likely the main

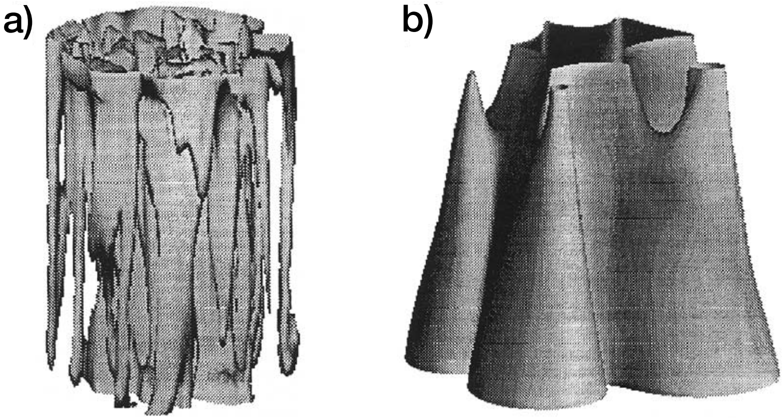

Fig. 2. Numerical simulations of ocean chimney convection from [31]. (a) Isotherm surfaces of small-scale helical vortices with central downwellings shortly after the onset of convection. (b) Isotherm surface showing pattern of baroclinic instability.

source of buoyancy driving the convection [25,26]. In the outer core the horizontal velocity is expected to be convergent near the inner core boundary and divergent near the core–mantle boundary. Accordingly, the thermal wind in the tangent cylinder is expected to be cyclonic (i.e. prograde, or eastward) near the inner core boundary and anticyclonic (i.e. retrograde, or westward) near the core–mantle boundary.

Under certain conditions the thermal wind is unstable. Instability of the thermal wind occurs through baroclinic waves, which develop when the buoyancy difference inside versus outside the chimney becomes sufficiently large. The instability begins as wave-like perturbations in the thermal wind along the outer edge of the chimney. As these waves grow they develop into baroclinic eddies (see Fig. 2b). The eddies tend to have a characteristic size, usually referred to as the Rossby deformation radius R_{D} [24]. In a rotating fluid layer with parallel top and bottom boundaries, the baroclinic eddies eventually separate from the large-scale thermal wind, and mix the chimney fluid into the external environment [27]. With boundary topography, however, the eddies tend to be topographically confined, and mixing between the chimney and its environment is less. For example, experiments by Whitehead [28] and Jacobs and Ivey [29] on rotating convection in the presence of a conical boundary showed that the baroclinic eddies tend to become trapped by the boundary topography, and instead of propagating outwards, drift in the thermal wind along the edge of the chimney.

The following similarity model has been used to characterize fully developed chimney convection [30–32]. The model assumes that the chimney buoyancy, the thermal wind, and the scales of the helical plumes and the baroclinic eddies depend only on the buoyancy flux averaged over the surface of the chimney B (with units m^2 s^{-3}), the chimney depth H and radius R, and the planetary rotation rate Ω (or alternatively the Coriolis parameter $f=2\Omega$). The model is intended for the asymptotic limit in which the convection is independent of the transport and thermodynamic properties of the fluid. This limit corresponds to low Ekman number and high Rayleigh number (as defined in the next section) and is considered to be the appropriate limit for convection in the outer core. In addition, this model assumes equilibrium conditions, in which the buoyancy flux into the chimney is balanced by the lateral loss of buoyancy through baroclinic instability. Such an equilibrium is a reasonable assumption for the slowly evolving core.

Dimensional analysis indicates that, under these conditions, the local buoyancy of the fluid in the chimney g' should scale as:

$$g' = \frac{\delta\rho}{\rho} g \sim (Bf)^{1/2} \tag{1}$$

Here g is gravitational acceleration and $\delta\rho/\rho$ is the fractional density difference between the fluid inside and outside the chimney. Dimensional analysis also indicates that the size of fully developed baroclinic instabilities should scale approximately with the Rossby deformation radius, which is given by:

$$R_D \sim \frac{(g'H)^{1/2}}{f} \tag{2}$$

Eliminating buoyancy from Eqs. 1 and 2 yields:

$$R_D \sim \left(\frac{BH^2}{f^3}\right)^{1/4} \tag{3}$$

In ocean convection, the helical plumes tend to be smaller in scale than the baroclinic eddies, and obey a different scaling law [22].

The azimuthal velocity in the thermal wind can be estimated using the thermal wind relationship [24]:

$$f\frac{\partial u}{\partial z} = \frac{\partial g'}{\partial s} \tag{4}$$

where u is the azimuthal velocity, z is the coordinate parallel to the rotation axis (antiparallel to gravity), and s is the coordinate normal to the rotation axis. Denoting the characteristic thermal wind velocity by U, the vertical length scale by H, and the horizontal length scale by R, Eqs. 1 and 4 combine to give the following scaling law for the thermal wind:

$$U \sim \frac{H}{R}\left(\frac{B}{F}\right)^{1/2} \tag{5}$$

In the Earth's core tangent cylinder and in our experiments, the fluid depth and radius are related by $H \simeq 2R$, in which case Eq. 5 reduces to:

$$U \sim 2\left(\frac{B}{f}\right)^{1/2} \tag{6}$$

3. Controlling parameters in rotating convection

The similarity model in the previous section is not a complete model for rotating convection, because it assumes that the buoyancy, the scale of the convection, and the thermal wind are all independent of the transport and thermodynamic properties of the fluid. The full theory of rotating convection includes the fluid transport and thermodynamic properties, and involves at least four dimensionless control parameters. For thermal convection, these are the Rayleigh number Ra, the Ekman number Ek, the Prandtl number Pr, and a geometrical parameter, in this case the radius ratio of the spherical shell η. Ranges of these four parameters in our experiments and their nominal values in the core are given in Table 1.

We characterize our experiments using a buoyancy flux Rayleigh number, defined as:

$$Ra = \frac{BH^4}{\kappa^2 \nu} \tag{7}$$

where κ is the diffusivity of buoyant constituent and ν is the kinematic viscosity of the fluid. The buoyant constituent in our experiments is heat and the diffusivity is thermal, so the buoyancy flux is:

$$B = \frac{\alpha g q}{\rho C_p} \tag{8}$$

where α is the thermal expansion coefficient, q is the average heat flux at the base of the tangent cylinder (in W m^{-2}), ρ is the fluid density, and C_p is the specific heat. It is usually assumed that the buoyancy of the outer core fluid is both thermal and compositional in origin, and is mainly a product of inner core growth [33,34]. Accordingly, the buoyancy flux at the inner core boundary can be expressed in terms of the rate of solidification of the inner core, as we show in Section 6.

Table 1
Non-dimensional parameter values in our experiments and estimated values for the Earth's core

Parameter	Experiments	Core
Ek	9×10^{-4}–10^{-5}	$<10^{-12}$
Ra	3×10^{6}–3×10^{10}	$>10^{20}$
Pr	7	$\sim10^{-2}$
η	0.33	0.35

The Ekman number is the ratio of viscous to Coriolis forces:

$$Ek = \frac{\nu}{fH^2} \tag{9}$$

written here in terms of the Coriolis parameter f. The Prandtl number is the ratio of kinematic viscosity to thermal diffusivity of the fluid:

$$Pr = \frac{\nu}{\kappa}. \tag{10}$$

Our experiments use water with $Pr \simeq 7$, whereas $Pr \simeq 0.01$ in the Earth's iron-rich outer core. Lastly, the spherical shell geometry of the tangent cylinder region of the outer core is described by the ratio of the inner core radius R to the outer core radius R_o:

$$\eta = \frac{R}{R_o} \tag{11}$$

4. Experimental apparatus and technique

Fig. 3 shows two schematic views of our experiment. A 35 cm diameter cylindrical tank is centered on the spin axis of an 82 cm diameter rotating table (the rotating table is described in [36]). A 30.4 cm diameter Plexiglas hemispherical cap, representing the core–mantle boundary, is centered inside the tank. The inner core boundary is modeled using a 10 cm diameter cylinder, also centered on the spin axis, and inserted through the base of the tank. The height of the insert cylinder above the base of the tank can be varied from flush (no basal topography) to 3.6 cm elevation (basal topography comparable to the inner core boundary). The top of the insert cylinder consists of a 6.4 mm thick heated copper disk, fastened by

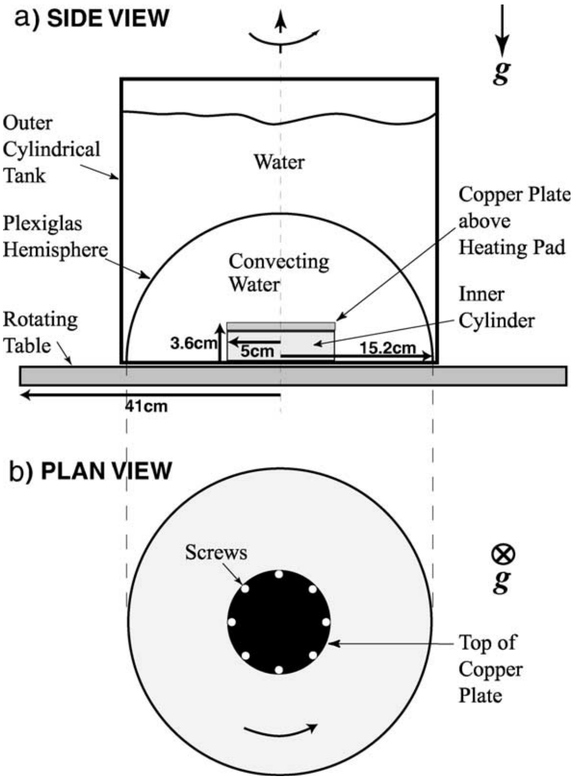

Fig. 3. Schematic illustrations of the experimental apparatus in (a) side view and (b) plan view.

eight stainless steel screws seen in Fig. 3b. The cylindrical radius of the copper disk and the spherical radius of the Plexiglas hemisphere cap are in the ratio 1:3, so that their relative dimensions are comparable to η, the ratio of inner core boundary to core–mantle boundary radii.

An electrical resistance heater is attached to the underside of the copper disk, and connected via a set of electrical slip rings to a power supply in the stationary frame. Insulation is placed around the heater assembly to ensure that a constant rate of heating is applied to the working fluid. In particular, the resistance heater is insulated from below and the copper disk is encased in a rubber seal designed to suppress lateral heat transfer to the fluid.

We have used a cylindrical geometry for the insert for dynamical reasons. The cylindrical side wall of the insert offers a topographic barrier to rotationally aligned, nearly 2D flow. This is comparable to the barrier offered by the spherical inner core to similar flows in the outer core. We tested a hemispherical insert, but found that it creates spurious baroclinic motions in the fluid, due to the misalignment between the isobars and isotherms near the heat source.

The experimental method is as follows. First, the cylindrical tank is filled with degassed water above the level of the hemisphere cap. The water above the cap acts to thermally insulate the fluid within the hemisphere. In experiments making use of flake visualization techniques, we inject the flakes into the fluid within the hemisphere prior to starting the rotation. The table is then rotated at a fixed angular velocity Ω for 30–60 min, in order for the fluid to reach solid body rotation. In experiments where the flow is visualized using fluorescein dye, we activate a dye injection pump located in the rotating frame after spin-up is complete. After solid body rotation is reached, the power is applied to the heater, resulting in a fixed total heat flux (and a nearly uniform buoyancy flux) into the overlying fluid. The resulting convective flows are recorded by a digital video camera mounted in the rotating frame, and by photographic images from both the stationary and rotating frames.

Note that the heat loss from the hemisphere is negligible, since the cap is effectively an insulator. Accordingly, the fluid within the hemisphere heats-up in the course of an experiment, and steady-state temperature conditions are not reached. This situation is analogous to the chemical evolution of the outer core in response to solidification of the inner core. The thermally insulating outer boundary in our experiment corresponds to zero mass flux at the core–mantle boundary, and the thermal buoyancy flux at the heater in our experiment corresponds to chemical buoyancy flux at the inner core boundary. In the core, the inner core growth rate and the chemical buoyancy flux into the outer core are ultimately controlled by the heat loss at the core–mantle boundary, whereas in our experiments the two boundary conditions are independent. However, in our experiments the time scale of the convection is short compared to the time scale of thermal evolution of the fluid as a whole, just as convection in the core is rapid compared to the rate of chemical evolution. Because of this difference in time scales, the system approaches an equilibrium, after an initial transient, in which the temperature anomaly in the chimney and the velocity of the thermal wind become essentially independent of time.

5. Results

5.1. Experiments without boundary topography

We made several initial experiments in a layer with a uniform depth of 4 cm, in order to delineate the influence of rotation without the inner core topography. We replaced the outer hemisphere with a flat cap in these experiments, and we positioned the heated surface of the insert cylinder flush with the base of the tank. This geometry allows us to compare our results with previous plane-layer studies. We examined plane-layer cases with and without rotation.

Fig. 4a shows the flow pattern in a plane-layer experiment without rotation. A single turbulent plume forms over the heater. The plume diverges on approach to the top boundary and spreads beyond the heater radius, while a return flow develops throughout the rest of the fluid. Fig. 4b,c shows two images from experiments in this same geometry with rotation added. Fig. 4b shows the planform shortly after onset of convection. A nearly uniform distribution of smaller-scale helical plumes fills the chimney region. Fig. 4c shows the planform after the chimney region has become baroclinically unstable. Baroclinic vortices pinch off from the chimney region and propagate outward along spiral trajectories. Note that the baroclinic vortices are larger in diameter than the initial scale of the helical plumes. Without boundary topography, we find that baroclinic instabilities transport the buoyant fluid away from the chimney region, and the lack of topography allows for lateral mixing in this case. This behavior is consistent with the numerical results of Jones and Marshall [31] for the plane-layer geometry shown in Fig. 2, as well as the experimental results of Maxworthy and Narimousa [32] and Jacobs and Ivey [30].

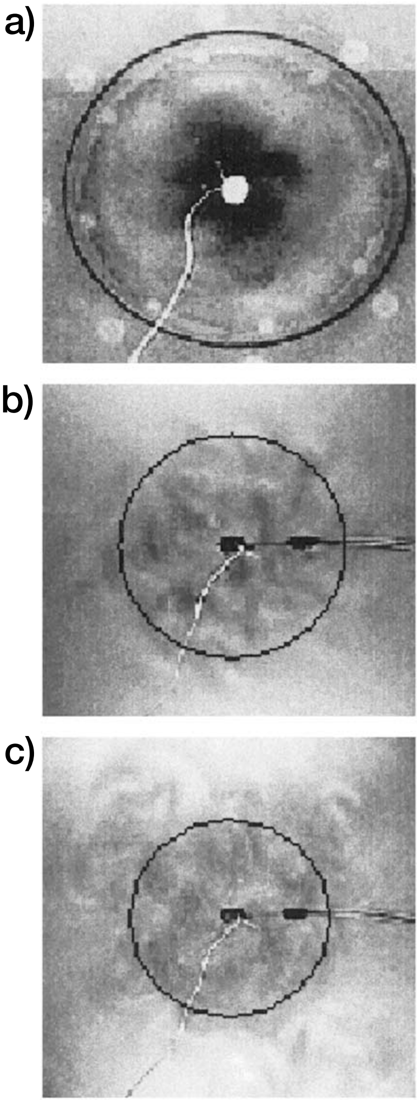

Fig. 4. Plan view images from plane-layer experiments. (a) Non-rotating case ($Ra = 1.13 \times 10^{10}$). Rotating case ($Ra = 5.17 \times 10^{8}$; $Ek = 5.47 \times 10^{-5}$), (b) shortly after the onset of convection and (c) after baroclinic instability. Black circles represent the outer circumference of the heated disk.

5.2. Experiments with boundary topography

We have made over 70 experiments with the geometry shown in Fig. 3 to establish how the

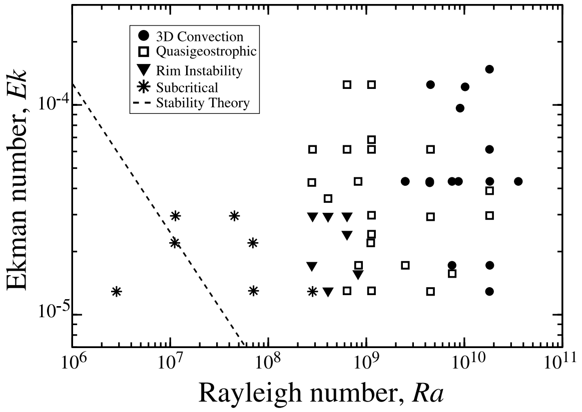

Fig. 5. Dominant style of chimney formation in tangent cylinder geometry as a function of Rayleigh and Ekman numbers. The dashed line denotes the onset of convection in an infinite plane layer with no-slip boundaries [35].

simultaneous effects of rotation and boundary topography affect the structure of the convection and the development of the chimney, over a wide parameter range. Our results delineate four main styles of chimney formation, as shown in Fig. 5. We have classified these in terms of their respective *Ra* values, because we were able to vary *Ra* over nearly four orders of magnitude, whereas we were able to vary *Ek* over a much more limited range. In order of increasing *Ra*, they are: subcritical (conductive), rim convection, quasigeostrophic convection, and 3D convection, respectively.

We have based our classification scheme on the dominant chimney-forming mechanism seen prior to the onset of baroclinic instability. The chimney-forming mechanism is readily imaged by our dye technique in the early stage of an experiment, because the dye is introduced while the fluid is in solid body rotation, and the first deviations from solid body rotation are the convective motions. Later on, the baroclinic instabilities interfere with visualizing the convection, although a close study of the videos indicates the two forms of motion co-exist throughout the duration of the experiment.

Images of 3D convection are shown in Fig. 6. The side view image in Fig. 6 shows the vertical structure of small-scale, 3D plumes that form at high heating rates ($Ra \sim 10^{10}$). In the first phase, the small-scale convection fills the chimney region inside the tangent cylinder. In the next stage, a retrograde azimuthal thermal wind flow develops inside the tangent cylinder below the hemispherical cap. The thermal wind velocity increases with time as the chimney fills with heated fluid and becomes more buoyant. In the final stage, the thermal wind undergoes baroclinic instability, fluid is exchanged across the tangent cylinder by baroclinic eddies, and the system approaches a statistical equilibrium (see Fig. 7c,d). In 3D convection, buoyancy forces are relatively large compared with Coriolis effects, so lateral mixing across the tangent cylinder is only slightly inhibited. The effect of rotation is too weak to prevent the baroclinic eddies from easily separating from the chimney and mixing with the fluid exterior to the tangent cylinder.

In experiments at lower Rayleigh numbers, near $Ra \simeq 10^{9}$ for example, smaller-scale quasigeostrophic convection occurs as helical plumes, rotationally aligned vortices with rising motion at their centers. The helical plumes have anticyclonic vorticity near the upper boundary where the flow is divergent and cyclonic vorticity near the heater where the flow is convergent. The particle trajectories in the plumes are helical, and the sign of the helicity changes where the vorticity reverses. Fig. 7 shows plan-view images of quasigeostrophic flow. The flow at the onset of convection is well-organized and evolves through a sequence of stages similar to the 3D regime. An upwelling cylindrical sheet first forms along the tangent cylinder as shown in Fig. 7a. Smaller diameter, concentric sheet-like upwellings then form above the heater. Soon after formation, these sheets become unstable to the wave-like disturbances shown in Fig. 7b. These waves are themselves unstable, and the sheet structures evolve into small-scale helical plumes that ascend vertically, filling the chimney region. The mature phase of this regime occurs after the chimney region fills with buoyant fluid. Six R_D-scale baroclinic eddies dominate the flow, as seen in Fig. 7c. The baroclinic eddies attempt to spread across the tangent cylinder in Fig. 7d but are mostly destroyed in the shear layer at the tangent cylinder.

Figs. 8 and 9 show convection at lower *Ra* and

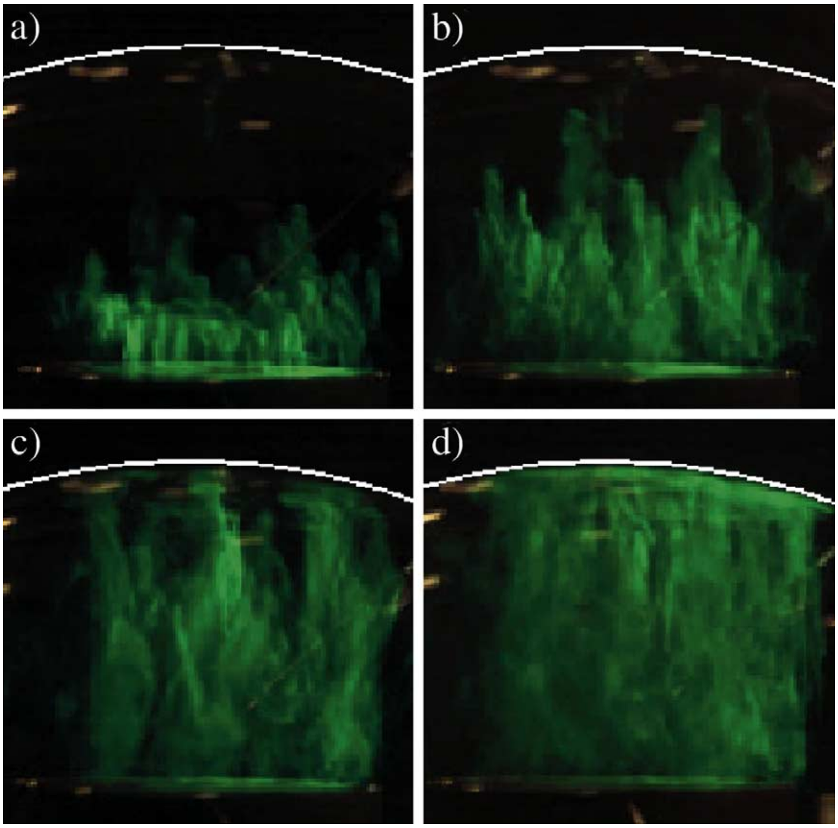

Fig. 6. Side view dye images of the 3D convection regime ($Ra = 1.10 \times 10^{10}$; $Ek = 4.11 \times 10^{-5}$). Images a, b, c, and d were taken 48, 64, 80 and 96 s after the onset of heating, respectively. (a) Small-scale 3D plumes, (b) plumes starting to be affected by rotation, (c) helical plumes, (d) fully developed tangent cylinder structure just before the onset of baroclinic instability. The dye was distributed over the planar top surface of the cylindrical insert prior to the onset of heating. The white arc marks the outer hemisphere boundary.

Ek, where the effect of rotation is stronger compared to the previous cases. Fig. 8 shows the helical plumes in side view. As can be seen in Fig. 9, fluid exchange between the chimney and its surroundings is weak, because the helical plumes are confined by the topographic step at the tangent cylinder.

At lower heating rates, around $Ra \simeq 5 \times 10^8$, helical plumes develop only along the tangent cylinder, due to edge effects of the heater. At this Rayleigh number the fluid inside the tangent cylinder is stable to convective motions. We refer to this style of flow as rim instability. When baroclinic instability occurs in this case, the eddies first migrate inwards, distributing heat over the interior of the tangent cylinder. Following the initial inward migration, weaker baroclinic motions transport some buoyant fluid to the tangent cylinder exterior. At still lower heating, around $Ra < 5 \times 10^7$, the fluid inside and outside the tangent cylinder is stable against convective motions, although a very weak thermal wind develops in response to diffusive thermal gradients in the fluid above the heater. This thermal wind tends to suppress convection, so the Rayleigh number for the onset of convection in this experiment is slightly higher than the critical Rayleigh number in an infinite plane layer at the same rotation rate.

Fig. 10 shows temperature records from an experiment at $Ra = 5.7 \times 10^9$ and $Ek = 2.8 \times 10^{-5}$, which resulted in a quasigeostrophic flow. These were recorded by thermistors located just below

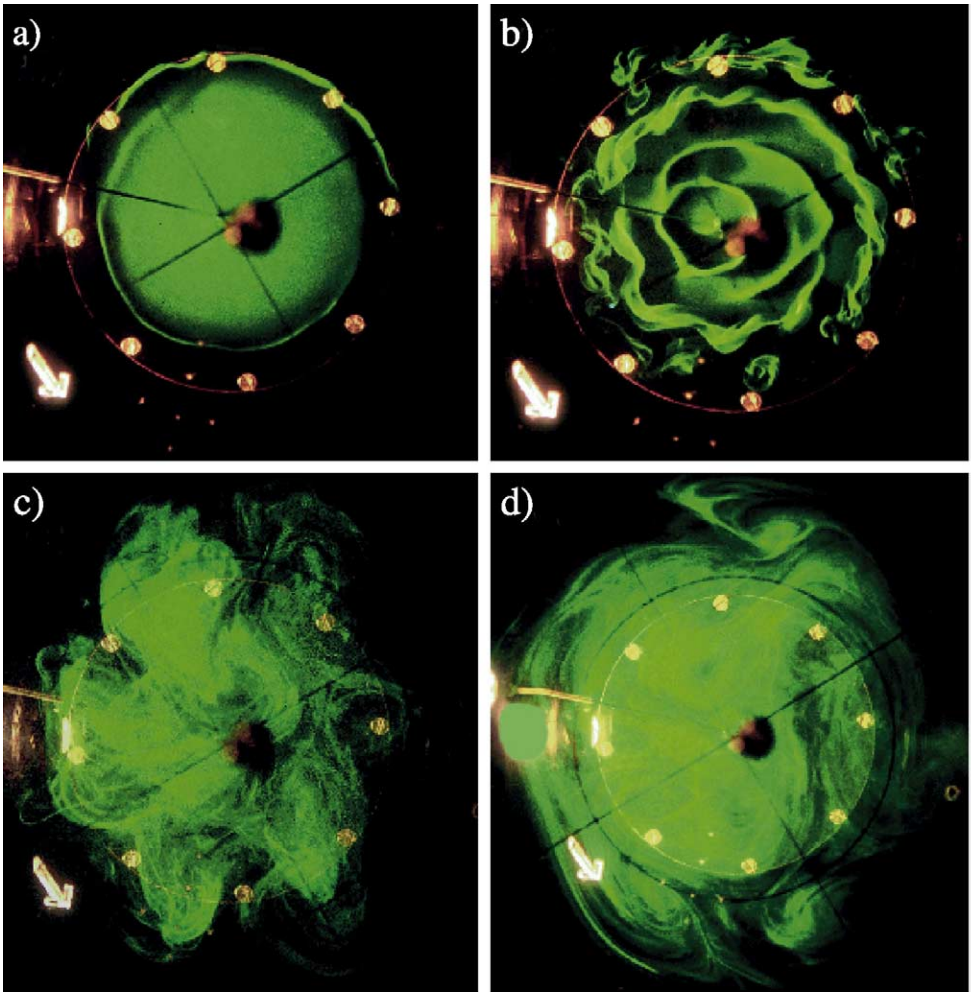

Fig. 7. Fluorescein dye images of helical plumes in plan view (experiment 42; $Ra = 9.01 \times 10^9$; $Ek = 9.65 \times 10^{-5}$). Images a–d were taken at between 1 and 8 min after the onset of heating. (a) Onset of convection, (b) helical plumes, (c) baroclinic instability, (d) fully developed baroclinic flow. Arrows indicate the direction of rotation.

the outer hemisphere boundary, at various latitudes along the same line of longitude. Thermistor 7 was located 1 cm of arc inside the tangent cylinder. Thermistor 8 was located on the tangent cylinder. Thermistors 9 and 10 were located 1 and 2 cm of arc outside of the tangent cylinder, respectively. The upward thermal spikes record upwelling helical plumes impinging on the outer boundary from below. The first plumes to reach the outer boundary ascend along the tangent cylinder, and are registered by spikes on thermistors 7, 8 and 9. The oscillatory signals are due to the passage of westward drifting helical plumes and baroclinic eddies. The oscillatory signal on thermistor 9 records the warm tangent cylinder fluid that geostrophically adjusts over a lateral distance of roughly one R_D. Thermistor 10, located outside the tangent cylinder, registers the first arrival of heated fluid approximately 7 min (over 110 rotations of the table) after the first arrivals are recorded on the three thermistors within the tangent cylinder. This time delay indicates the heated fluid within the chimney is strongly inhibited from crossing the tangent cylinder.

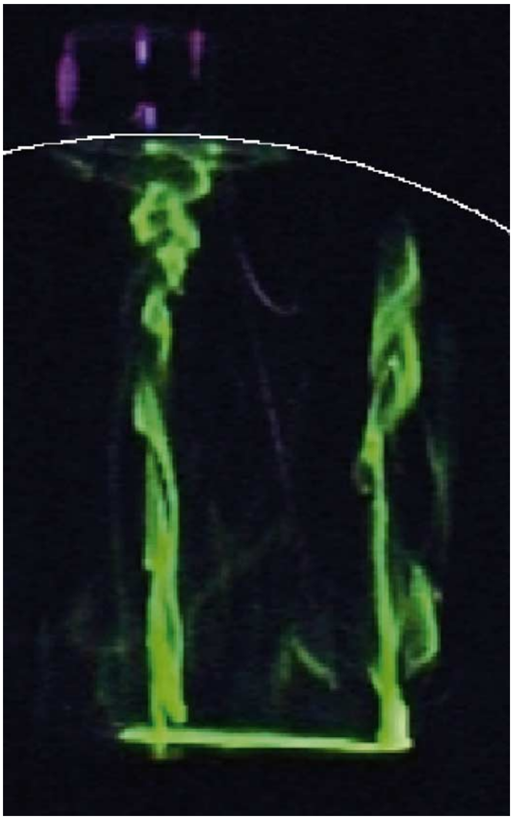

Fig. 8. Side view image showing helical plume structure shortly after the onset of convection ($Ra = 4.44 \times 10^9$; $Ek = 4.26 \times 10^{-5}$). The white arc marks the outer hemisphere boundary.

5.3. Thermal wind velocity and eddy size

Fig. 11 shows the average westward thermal wind velocity U measured along the tangent cylinder just below the outer hemisphere cap versus the velocity scale $\sqrt{B/f}$. These velocity measurements were made using digital video recordings of the experiments, by tracking dye filaments traveling along the tangent cylinder for at least 90° of arc. Each point in Fig. 11 corresponds to the average of two to four such velocity measurements taken in close succession. The solid line in Fig. 11 represents the following best-fit power-law to the azimuthal velocity measurements:

$$U = 2.05[(B/f)^{1/2}]^{1.04 \pm 0.06} \qquad (12)$$

with a correlation coefficient of 0.90. Both coefficient and the power-law exponent in Eq. 12 are consistent with Eq. 6, the predictions of the similarity model, to within experimental error. We observed that U initially increases with time and then plateaus towards a quasi-steady value over the course of each individual experiment. This behavior is expected, because the buoyancy of the chimney initially increases with time as its temperature rises relative to the surrounding fluid. At much later times, warmed fluid is exchanged with the surrounding environment and the temperature difference across the tangent cylinder becomes nearly constant. This secular heating effect can be seen by comparing thermistor 7 and 10 records in Fig. 10. Thus, some of the scatter in Fig. 11 can be accounted for by the secular velocity increase during an experiment and by measurement error in tracing short-lived dye filaments in the digital video recordings. Azimuthal velocity measurements were limited to the region immediately below the outer hemispherical cap, but below the Ekman boundary layer. Although quantitative velocity measurements at greater depths were not made, visual observations of dye streaks indicate that the azimuthal flow tends towards much weaker values with increasing depth in the chimney, as expected for a baroclinic thermal wind.

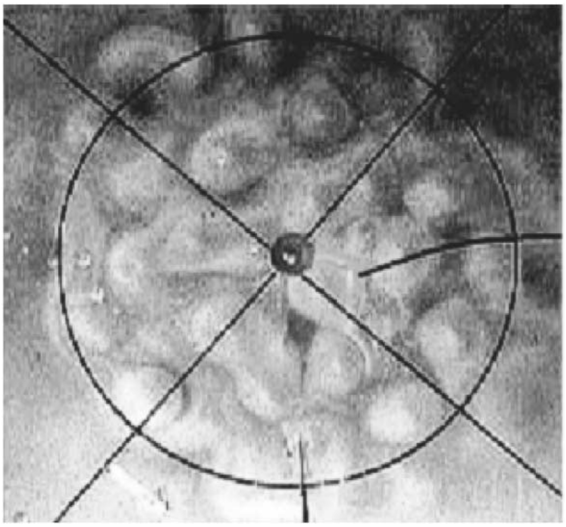

Fig. 9. Plan view image of helical plume convection ($Ra = 1.11 \times 10^9$; $Ek = 2.20 \times 10^{-5}$).

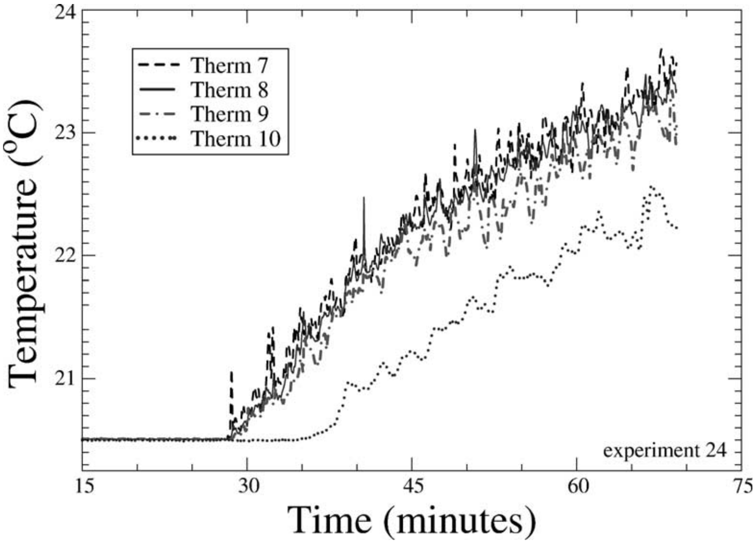

Fig. 10. Temperature records with helical plume convection ($Ra = 5.74 \times 10^9$; $Ek = 2.84 \times 10^{-5}$). The thermistors are situated just below the outer hemisphere boundary at the same longitude. Thermistors 7 and 8 are located 1 cm within and along the tangent cylinder, respectively. Thermistors 9 and 10 are located 1 cm and 2 cm outside the tangent cylinder, respectively.

Measurements were also made of baroclinic eddy and helical plume diameters using the digital video recordings. We observed that eddy diameters were of the same order of magnitude as the Rossby deformation radius, but because of two effects, we were unable to establish a scaling law for these structures. First, similarly to the velocity measurements, the eddy and plume diameters increased in time with the buoyancy within the tangent cylinder. Second, the separation of scales was not large between the eddies and the plumes (see Fig. 7). In our measurements the helical plumes were smaller in scale than the fully developed baroclinic eddies, in qualitative agreement with the results of previous studies of ocean convection [22]. However, the plume sizes were also quite variable, and we were formally unable to distinguish the eddy population from the helical plumes population.

6. A relationship between convection and thermal wind in Earth's core tangent cylinder

Our experiments suggest a simple relationship between thermal wind velocity and buoyancy flux due to convection in the tangent cylinder (Eq. 12) which is consistent with the scaling arguments proposed in Section 2. This relationship can be applied to the core, since it involves only the buoyancy flux at the inner core boundary and the thermal wind velocity below the core–mantle

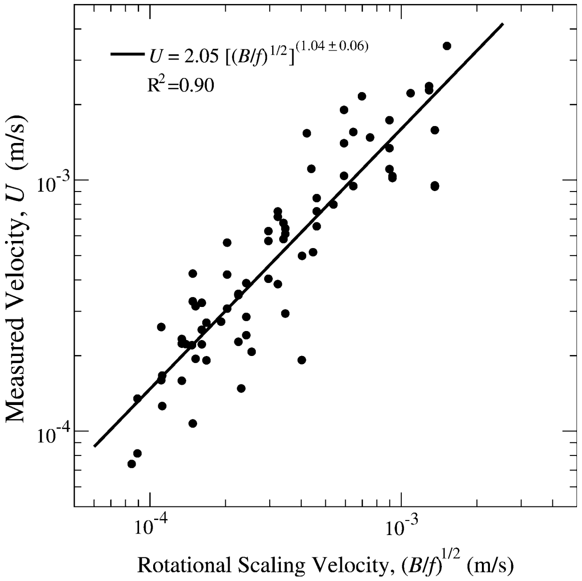

Fig. 11. Retrograde thermal wind velocity on the tangent cylinder versus the scaling velocity.

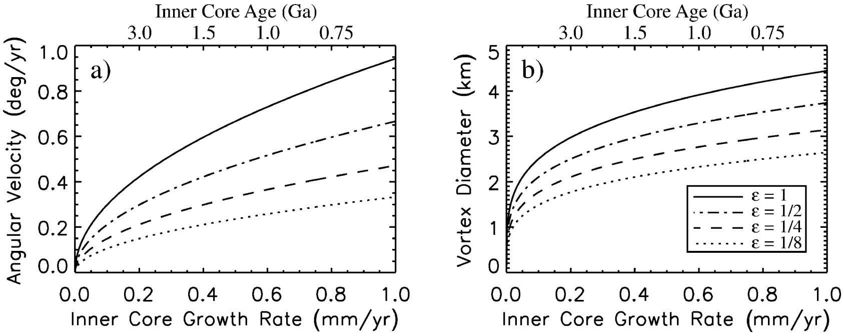

Fig. 12. (a) Angular velocity on Earth's core tangent cylinder versus inner core growth rate from Eq. 19; (b) approximate baroclinic convective vortex diameter (R_D) versus inner core growth rate. Equivalent inner core ages assume $t^{1/2}$ growth.

boundary, both of which have been estimated previously using independent techniques. Equally important, Eq. 12 is independent of the transport properties of the fluid (viscosity and diffusivity), which are notoriously uncertain in the outer core. Even so, several assumptions must be made about convection in the outer core that are difficult to verify. First, we assume that the convection in the tangent cylinder of the outer core, which is likely driven by thermal and compositional effects, obeys the same scaling law as the thermal convection in our experiments (that is, it depends only on the buoyancy flux, not the source of the buoyancy). Second, we neglect the effects of Lorentz forces and compressibility, which may affect the thermal wind velocity. Third, we must assume that a certain fraction ε of the buoyancy produced at the inner core boundary remains within the tangent cylinder region to drive the convection there. Since this fraction is unknown, we calculate the thermal wind for values of this parameter between zero and one.

The energetics of the core indicate that the buoyancy flux at the inner core boundary includes both thermal and compositional parts [25,26]. The most important source of thermal buoyancy is latent heat release, and the most important source of compositional buoyancy is chemical differentiation [33]. Each of these sources of buoyancy is proportional to the rate of inner core solidification.

The compositional buoyancy flux at the inner core boundary is due to the rejection of lower density, iron-depleted liquid during the solidification of the inner core. This iron-depleted liquid is less dense than both the solid inner core and the liquid outer core, and hence are gravitationally unstable at the inner core boundary. If $\Delta\rho$ now denotes the density difference between the outer core and this liquid (measured at the inner core boundary temperature and pressure), then the compositional buoyancy of the liquid rejected at the inner core boundary is given by:

$$g'_C = \frac{\Delta\rho}{\rho} g \tag{13}$$

where ρ and g now denote liquid density and gravity, respectively, at the inner core boundary. The buoyancy of this liquid due to latent heat release at the inner core boundary is given by:

$$g'_L = \frac{\alpha L}{C_p} g \tag{14}$$

where L is the latent heat of melting (in J kg^{-1}), C_p is specific heat and α is thermal expansion. The total fluid buoyancy at the inner core boundary g'_i is just the sum of Eqs. 13 and 14:

$$g'_i = \left(\frac{\Delta\rho}{\rho} + \frac{\alpha L}{C_p}\right) g \tag{15}$$

A simple model for the buoyancy flux at the inner core boundary assumes it is proportional to the rate of inner core growth [25,26], i.e.:

$$B_i = g'_i \frac{dR}{dt} \tag{16}$$

where R now denotes the inner core radius and t is time. The average buoyancy flux entering the base of one tangent cylinder region (northern or southern) is then:

$$B = 2\varepsilon g'_i \frac{\mathrm{d}R}{\mathrm{d}t} \tag{17}$$

The factor 2 appears in this expression because the surface area of one hemisphere of the inner core boundary is twice the cross sectional area of its respective tangent cylinder. The scaling law for thermal wind (Eq. 12) can be written in terms of angular velocity on the core tangent cylinder ω as:

$$\omega \simeq 2c\left(\frac{B}{f}\right)^{1/2} \tag{18}$$

where the factor $c = 1480$ deg·s/m·yr converts from *m/s* to *deg/yr* in Eq. 18. In writing Eq. 18 we have taken the power-law exponent in Eq. 12 to be one and the coefficient to be two, as in Eq. 6. Eqs. 17 and 18 can be combined to give the angular velocity of the thermal wind on the tangent cylinder as a function of the inner core growth rate. The result simplifies to:

$$\omega \simeq 2c\left(\frac{\varepsilon g'_i}{\Omega}\frac{\mathrm{d}R}{\mathrm{d}t}\right)^{1/2} \tag{19}$$

where we have used $f = 2\Omega$.

Fig. 12a shows the thermal wind angular velocity ω as a function of inner core growth rate for various values of ε, according to Eq. 19. The curves were calculated using the core parameter values given in Table 2. Fig. 12 also shows equivalent inner core ages, calculated assuming the inner core has grown as $\sqrt{t}$. In Table 2 we give the range of inner core growth rates estimated from various evolution models of the core [33]. The lower end of this range corresponds to old inner core ages ($\simeq$4 Ga), while the upper end corresponds to relatively young ages ($\simeq$0.5 Ga). In Table 2 we also give the range of westward angular velocity in the two large-scale polar vortices inferred from geomagnetic secular variation on the core–mantle boundary at high latitude [19,20].

The thermal wind angular velocity in the tangent cylinder is proportional to the square root of the inner core growth rate. For example, if we assume $\varepsilon = 0.5$ (which is equivalent to assuming that one quarter of inner core buoyancy flux enters each of the two tangent cylinder regions), then the predicted thermal wind angular velocity in the tangent cylinder is about 0.35° yr^{-1} if $\mathrm{d}R/\mathrm{d}t = 0.3$ mm yr^{-1} (2 Ga inner core age), or about 0.65° yr^{-1} if $\mathrm{d}R/\mathrm{d}t = 0.9$ mm yr^{-1} (667 Ma inner core age). These predicted velocities are comparable to (although somewhat smaller than) the average angular velocity in the core tangent cylinder inferred from present-day geomagnetic secular variation, as given in Table 2. From this comparison, we conclude that the inferred large-scale polar vortices in the Earth's core are consistent with a thermal wind driven by inner core growth, provided a substantial fraction of the buoyancy released by inner core growth remains within the

Table 2
Core properties (the abbreviation 'ICB' denotes the inner core boundary)

Property	Symbol	Units	Value	Reference
thermal expansion	α	K^{-1}	1×10^{-5}	[33]
ICB gravity	g	$\mathrm{m\ s}^{-2}$	4.4	[33]
ICB density	ρ	$\mathrm{kg\ m}^{-3}$	12×10^{3}	[33]
ICB density jump (comp)	$\Delta\rho$	$\mathrm{kg\ m}^{-3}$	0.5×10^{3}	[32]
ICB latent heat	L	$\mathrm{J\ kg}^{-1}$	5×10^{5}	[33,34]
specific heat	C_p	$\mathrm{J\ kg}^{-1}\ \mathrm{K}^{-1}$	660	[32]
angular rotation velocity	Ω	s^{-1}	7.292×10^{-5}	[33]
Coriolis parameter	$f = 2\Omega$	s^{-1}	1.458×10^{-4}	[33]
ICB radius	R	m	1.22×10^{6}	[33]
thermal diffusivity	κ	$\mathrm{m}^2\ \mathrm{s}^{-1}$	$\sim10^{-5}$	[32]
viscosity	ν	$\mathrm{m}^2\ \mathrm{s}^{-1}$	$\sim10^{-7}$	[33]
IC growth rate	$\mathrm{d}R/\mathrm{d}t$	$\mathrm{mm\ yr}^{-1}$	0.15–0.8	[32]
polar vortex angular velocity (ave)	ω	$^\circ\ yr^{-1}$	0.3–0.6	[19,20]

tangent cylinder ($\varepsilon \simeq 0.5$), and provided the rate of inner core growth is relatively high.

We find that the baroclinic vortex size in our experiments scales approximately with the Rossby deformation radius, according to $R_D \sim (BH^2/f^3)^{1/4}$. In Fig. 12b, we estimate the typical tangent cylinder baroclinic vortex diameter to be of the order R_D and plot this quantity versus inner core growth rate for various values of ε, using the parameter values in Table 2. For typical inner core growth rates, the results in Fig. 12b indicate that tangent cylinder vortices have diameters near 2 km. Lastly, we use Eqs. 17, 7, and 1 to estimate order-of-magnitude values for the tangent cylinder buoyancy flux, Rayleigh number and the density anomaly between the tangent cylinder fluid versus the rest of the core, respectively. Assuming $\varepsilon = 0.5$ and $dR/dt = 0.3$ mm yr^{-1}, Eq. 17 gives $B \simeq 10^{-12}$ m^2 s^{-3}, Eq. 7 gives $Ra \simeq 10^{31}$, and Eq. 1 gives $\delta\rho \simeq 10^{-4}$ kg m^{-3}.

It is also possible to estimate the compositional anomaly between the tangent cylinder and the surrounding core fluid from the results of our experiments. Suppose that the core is a mixture of Fe and a light compound, say FeS (the particular choice of light compound is not essential to our argument). Let χ denote the mass fraction of the light compound (i.e. FeS) outside the tangent cylinder, while ζ denotes the mass fraction of light compound inside the tangent cylinder. Then, the compositional anomaly of the tangent cylinder is given by:

$$\zeta - \chi = \left(\frac{\delta\rho}{\rho}\right)\left(\frac{1-\chi\rho_{\mathrm{Fe}} + \chi\rho_{\mathrm{FeS}}}{\rho_{\mathrm{Fe}} - \rho_{\mathrm{FeS}}}\right) \qquad (20)$$

where ρ_{Fe} and ρ_{FeS} are the density of Fe and FeS liquids, respectively. Linearly extrapolating density measurements made at 30 GPa and 1800 K [37] and assuming that $\chi \simeq 0.10$, we estimate from Eq. 20 a compositional anomaly across the tangent cylinder of $\zeta - \chi \simeq 5 \times 10^{-8}$.

7. Summary

We have identified four styles of buoyantly driven flow in the geometry of the Earth's core tangent cylinder. With increasing Rayleigh number these are: weak thermal wind driven by conduction (no convection), convection along the tangent cylinder, quasigeostrophic convection, and 3D turbulent convection. A westward azimuthal thermal wind flow is observed below the core–mantle boundary in all cases, although it is strong only in the presence of convection. Our experiments show that the azimuthal velocity of the thermal wind scales with average buoyancy flux of the convection and the rotation rate, according to $U \sim 2(B/f)^{1/2}$.

We find that the large-scale geomagnetically inferred polar vortices in the outer core can be explained as thermal winds driven by buoyancy produced at the inner core boundary if the inner core growth rate is high and if a substantial fraction of the buoyant fluid produced at the inner core boundary remains within the tangent cylinder region. In addition, we infer that the diameters of convective elements in the tangent cylinder (baroclinic vortices) are on the order of a few kilometers, and that the flux Rayleigh number there is of the order of 10^{31}. If the tangent cylinder acts as a barrier to mixing as in our experiments, we expect undetectably small density and compositional differences to exist between the fluid inside the tangent cylinder and the rest of the outer core.

Our experimental results for thermal wind velocity are consistent with an asymptotic scaling law that is independent of transport properties such as viscosity and thermal or chemical diffusivity. This offers some advantage for extrapolation to the Earth's core, where transport properties are poorly known. Therefore, it would be of interest to compare our results with numerical dynamo simulations and magnetohydrodynamics experiments using liquid metals, to determine how these scaling laws are modified by magnetic fields, compressibility, and other effects we have not considered.

Acknowledgements

This research has been supported by the Geophysics Program of the National Science Foundation. Support for J.A. has also been provided under NASA Grants NAG5-4077 and NAG5-10165.***[SK]***

References

[1] E. Dormy, A.M. Soward, C.A. Jones, D. Jault, P. Cardin, The onset of thermal convection in rotating spherical shells, J. Fluid Mech. (2003) in press.

[2] C.R. Carrigan, F.H. Busse, An experimental and theoretical investigation of the onset of convection in rotating spherical shells, J. Fluid Mech. 126 (1983) 287–305.

[3] P. Cardin, P. Olson, Chaotic thermal convection in a rapidly rotating spherical shell: consequences for flow in the outer core, Phys. Earth Planet. Sci. 82 (1994) 235–259.

[4] M. Kono, P.H. Roberts, Recent geodynamo simulations and observations of the geomagnetic field, Rev. Geophys. 42, 1013, doi 10.1029, 2000RG000102.

[5] N.G. Hogg, H.M. Stommell, The Heton, an elementary interaction between discrete baroclinic geostrophic vortices and its implications concerning eddy heat-flow, Proc. R. Soc. London A 397 (1985) 1–20.

[6] J.M. Aurnou, D. Brito, P. Olson, Anomalous rotation of the inner core and the toroidal magnetic field, J. Geophys. Res. 103 (1998) 9721–9738.

[7] G.A. Glatzmaier, P.H. Roberts, A three-dimensional self-consistent computer simulation of a geomagnetic reversal, Nature 377 (1995) 203–208.

[8] U.R. Christensen, P. Olson, G.A. Glatzmaier, A dynamo model interpretation of geomagnetic field structures, Geophys. Res. Lett. 25 (1998) 1565–1568.

[9] G.A. Glatzmaier, P.H. Roberts, Rotation and magnetism of Earth's inner core, Science 274 (1996) 1887–1891.

[10] J.M. Aurnou, D. Brito, P.L. Olson, Mechanics of inner core super-rotation, Geophys. Res. Lett. 23 (1996) 3401–3404.

[11] X.D. Song, P.G. Richards, Seismological evidence for differential rotation of the Earth's inner core, Nature 382 (1996) 221–224.

[12] K.C. Creager, Inner core rotation rate from small-scale heterogeneity and time-varying travel times, Science 278 (1997) 1284–1288.

[13] X.D. Song, A. Li, Support for differential inner core superrotation from earthquake in Alaska recorded at South Pole station, J. Geophys. Res. 105 (2000) 623–630.

[14] J.E. Vidale, D.A. Dodge, P.S. Earle, Slow differential rotation of the Earth's inner core indicated by temporal changes in scattering, Nature 405 (2000) 445–448.

[15] A. Souriau, New seismological constraints on differential rotation of the inner core from Novaya Zemlya events recorded at DRV, Antarctica, Geophys. J. Int. 134 (1998) F1–F5.

[16] G. Laske, G. Masters, Rotation of the inner core from a new analysis of free oscillations, Nature 402 (1999) 66–69.

[17] G. Poupinet, A. Souriau, O. Coutant, The existence of an inner core super-rotation questioned by teleseismic doublets, Phys. Earth Planet. Int. 118 (2000) 77–88.

[18] J. Tromp, Inner core anisotropy and rotation, Annu. Rev. Earth Planet. Sci. 29 (2001) 47–69.

[19] G. Hulot, C. Eymin, B. Langlais, M. Mandea, N. Olsen, Small-scale structure of the geodynamo inferred from Oersted and Magsat satellite data, Nature 416 (2002) 620–623.

[20] P.L. Olson, J.M. Aurnou, A polar vortex in the Earth's core, Nature 402 (1999) 170–173.

[21] A. Pais, G. Hulot, Length of day decade variations, torsional oscillations and inner core superrotation: evidence from recovered core surface zonal flows, Phys. Earth Planet. Int. 118 (2000) 291–316.

[22] J. Marshall, F. Schott, Open-ocean convection: observations, theory and models, Rev. Geophys. 37 (1999) 1–64.

[23] S. Legg, J. Marshall, A heton model of the spreading phase of open-ocean deep convection, J. Phys. Oceanogr. 23 (1993) 1040–1056.

[24] A. Gill, Dynamics of Atmospheres and Oceans, International Geophysics Series V30, Academic Press, 1982, 662 pp.

[25] J.R. Lister, B.A. Buffett, The strength and efficiency of thermal and compositional convection in the geodynamo, Phys. Earth Planet. Int. 91 (1995) 17–30.

[26] S.I. Braginsky, P.H. Roberts, Equations governing Earth's core and the geodynamo, Geophys. Astrophys. Fluid Dyn. 79 (1995) 1–97.

[27] T. Maxworthy, Convection into domains with open boundaries, Annu. Rev. Fluid Mech. 29 (1997) 327–371.

[28] J.A. Whitehead, A laboratory model of cooling over the continental shelf, J. Phys. Oceanogr. 23 (1993) 2412–2427.

[29] P. Jacobs, G. Ivey, The influence of rotation on shelf convection, J. Fluid Mech. 369 (1998) 23–48.

[30] P. Jacobs, G. Ivey, Rossby number regimes for isolated convection in a homogeneous, rotating fluid, Dyn. Atm. Ocean 30 (1999) 149–171.

[31] H. Jones, J. Marshall, Convection with rotation in a neutral ocean: A study of deep-ocean convection, J. Phys. Oceanogr. 23 (1993) 1009–1039.

[32] T. Maxworthy, S. Narimousa, Unsteady, turbulent convection in a homogeneous rotating fluid, with oceanographic applications, J. Phys. Oceanogr. 24 (1994) 865–887.

[33] B.A. Buffett, Dynamics of the Earth's Core, in: Earth's Deep Interior: Mineral Physics and Tomography from the Atomic to the Global Scale, Geophys. Monogr. Am. Geophys. Union 117 (2000) 37–61.

[34] F.D. Stacey, Physics of the Earth, Brookfield Press, Brisbane, 1992, 511 pp.

[35] S. Chandrasekhar, Hydrodynamic and Hydromagnetic Stability, Oxford University Press, Oxford, 1961, 654 pp.

[36] J.M. Aurnou, P.L. Olson, Experiments on Rayleigh-Benard convection, magnetoconvection and rotating magnetoconvection in liquid gallium, J. Fluid Mech. 430 (2001) 283–307.

[37] A. Kavner, T.S. Duffy, G. Shen, Phase stability and density of FeS at high pressures and temperatures: implications for the interior structure of Mars, Earth Planet. Sci. Lett. 185 (2001) 25–33.